Investigation of CsPbBr$_3$ CVD dynamics at various temperatures†

Chenyang Bao, Xiang Peng, Leiying Ying, Yang Mei, Baoping Zhang and Hao Long [ID] *

Since the emerging development of CsPbBr$_3$ perovskite, chemical vapor deposition (CVD) has become one of the most promising fabrication techniques by which to precisely deposit uniform perovskite thin films. However, there have been few reports on the growth dynamics and chemical reaction parameters (e.g., activation energy) for perovskite CVD. In this work, different deposition rates of CVD-grown CsPbBr$_3$ thin films were obtained at different substrate temperatures. Dynamics equations were developed to relate the inflow rates, desorption coefficients and concentrations of reactants on the substrates. Only a small amount of reactant became activated at low temperature and a small amount of PbBr$_2$ resided on the substrate at high temperature, and accordingly the maximal deposition rate was achieved at 250 °C. The Arrhenius activation energy of CVD-grown CsPbBr$_3$ was also calculated, and found to be 31.64 kJ mol^{-1}. We believe that our work provides a detailed picture of perovskite CVD growth.

Introduction

Since lead-halide perovskite (APbX$_3$) was first demonstrated in 2009,[1] this materials system has been extensively studied and applied in solar cells,[2,3] light-emitting devices,[4,5] photo detectors,[6] lasers,[7] etc. During the decade since, the certified power conversion efficiency levels of perovskite solar cell have surged to 25%.[8] Of all of the lead-halide perovskites, CsPbBr$_3$ has been recognized to be promising for producing bright green emitters, due to its environmental stability, strong exciton oscillation and high efficiency.[9–11] Although spin coating is currently widely adopted to synthesize CsPbBr$_3$,[12] the sensitivity of the environment to CsPbBr$_3$ and the inability to achieve a mass production of CsPbBr$_3$ in this manner have hindered industrialization of this technique. Meanwhile, chemical vapor deposition (CVD) is a widely accepted method for mass-producing semiconductor thin films in a controllable fabrication, due to its vacuum process and high precision. In the last few years, several works on CVD-grown CsPbBr$_3$ have been reported.[13–15] However, to date, there have been very few reports providing an in-depth understanding of CsPbBr$_3$ CVD dynamics. The physical modes (e.g., source transportation and reaction mechanism) of this fabrication have not been developed. Therefore, in this work, CsPbBr$_3$ thin films were grown

using CVD systems with two heater zones, at substrate temperatures of 30 °C to 300 °C. Dynamics equations of the reactants CsBr and PbBr$_2$ were calculated. Parameters including inflow of reactants, desorption coefficient, and concentrations of reactants on the substrates were derived. The highest deposition rate was achieved at a 250 °C substrate temperature. The lower deposition rates at temperatures lower than 250 °C were apparently due to limited reaction coefficients at such temperatures, whereas the lower deposition rates at temperatures higher than 250 °C were apparently due to the higher PbBr$_2$ desorption coefficients at such temperatures. The activation energy (31.64 kJ mol^{-1}) of the chemical reaction in the CVD system was also derived.

Experimental

Two individual furnaces were deployed as heat reactors using a 1:1 molar ratio of CsBr to PbBr$_2$ and quartz substrates, respectively, as shown in Fig. 1. A temperature of 500 °C was used to sublimate the sources, while various temperatures (30, 100, 150, 200, 250, 300 °C) were used for the quartz substrates. Nitrogen at 30 sccm was used as the carrier gas to transport the reactants onto the substrates. During growth, CsBr reacted with PbBr$_2$ to form CsPbBr$_3$, along with desorption from substrates as a result of thermal vibration. A pressure of 1300 Pa was set by using the valve between the vacuum pump and reactor chamber. X-Ray diffraction (XRD) phase analysis ($2\theta \sim \omega$) with 2θ from 10°–32° was performed

School of Electronic Science and Engineering (National Model Microelectronics College), Xiamen University, Xiamen, Fujian, 361005, People's Republic of China. E-mail: longhao@xmu.edu.cn

† Electronic supplementary information (ESI) available. See DOI: 10.1039/d1cp03794c

using a Bruker-AXS X-ray diffractometer. Surface scanning electron microscopy (SEM) images were acquired by using a Carl Zeiss apparatus (Sigma-HD). Thicknesses of deposition thin films were measured by using a step profiler (Bruker Dektak-XT). A photoluminescence (PL) spectrum was recorded by using an Andor spectrograph and charge-coupled device (CCD) excited by a 405 nm-wavelength continuous wave laser. X-Ray photoelectron spectroscopy (XPS) data were collected using an Escalab Xi+ apparatus (Thermo Fisher).

substrates, chemical reactions, surface desorption, *etc.* Any of these processes may impact the final thin films. Therefore, in this work, we considered three main processes—namely the inflow of reactants, the chemical reaction, and the desorption of sources—occurring on the substrate to interpret the experimental deposition rates R at various temperatures.

The dynamics processes for CsBr and PbBr$_2$ on substrate are illustrated in Fig. 1, and could be expressed as

$$\begin{cases} I_{CsBr}\left(P, T_{sub}, n_{CsBr}^c, n_{CsBr}^{sub}\right) - \alpha_{CsBr}(T_{sub}) \cdot n_{CsBr}^{sub} = R\left(T_{sub}, \mu, n_{CsBr}^{sub}, n_{PbBr_2}^{sub}\right) \\ I_{PbBr_2}\left(P, T_{sub}, n_{PbBr_2}^c, n_{PbBr_2}^{sub}\right) - \alpha_{PbBr_2}(T_{sub}) \cdot n_{PbBr_2}^{sub} = R\left(T_{sub}, \mu, n_{CsBr}^{sub}, n_{PbBr_2}^{sub}\right) \end{cases}. \quad (1)$$

After 20 minutes of CVD growth, CsPbBr$_3$ thin films were deposited on quartz substrates. Fig. 2 shows the phase analysis and PL spectrum of typical CsPbBr$_3$ thin films. As shown in Fig. 2a, all materials deposited using CVD appeared as an almost pure CsPbBr$_3$(110) phase, showing no parasitic products (*e.g.*, Cs$_4$PbBr$_6$ or CsPb$_2$Br$_5$). Under 405 nm-wavelength laser excitation, the CsPbBr$_3$ films emitted green light centered at 532 nm in the PL spectrum. Chemical stoichiometric ratio here was confirmed using XPS, as shown in (ESI†). Average crystalline size, dislocation density and strain of perovskite could be calculated based on the diffraction angle and width of XRD curves.[16–18] As shown in ESI,† CsPbBr$_3$ thin films deposited at 200 °C displayed the lowest dislocation density.

Fig. 3 shows the surface morphologies of CsPbBr$_3$ films visualized using SEM. Under high magnification (1000×), the CsPbBr$_3$ thin films appeared to be uniform and compact. As the temperature was increased to 250 °C, the grain size of CsPbBr$_3$ gradually increased, as shown in the inset. CsPbBr$_3$ grown at 30 °C and 300 °C both showed small discrete crystal particles. However, different morphologies resulted from the use of different substrate temperatures. As the substrate temperature is varied from 30 °C to 300 °C, the chemical reaction, diffusion and desorption coefficients of the reactants all diverge, inducing different crystal grains and deposition rates. A step profiler was used to measure the thicknesses of the deposited films for the purpose of calculating deposition rates. Step scanning profiles are shown in Fig. 3e. CsPbBr$_3$ films deposited at 250 °C were thickest, with a thickness of 420 nm.

CVD is a hybrid deposition system, involving sublimation and mass transport of reactants, diffusion of sources towards

The reactant inflow (I) was consumed either by desorption (α) or deposition (R). The rate of inflow of the reactants was determined from the diffusion coefficient (D), diffusion boundary thickness (δ) and concentrations of the source on the substrate (n^{sub}) and in the chamber (n^c) by using the equation

$$I = \frac{D}{\delta} \cdot \left(n^c - n^{sub}\right) \quad (2)$$

The reactant concentration (n^c) in the chamber was calculated based on the gas/liquid phase equilibrium equation $\ln\frac{P_c}{P_1} = \frac{\Delta_{vap}H_m}{R}\left(\frac{1}{T_1} - \frac{1}{T_c}\right)$ and ideal gas state equation $PV = nRT$. In these equations, $\Delta_{vap}H_m$ and R denote the molar vaporization enthalpy and molar gas constant, respectively, P_c and T_c denote, respectively, the pressure and temperature in the chamber (with T_c set to 500 °C), and (P_1, T_1) denotes any known vaporization point on the phase equilibrium line. The diffusion coefficient (D) could be calculated by using the equation $D = \frac{1}{3}\bar{\nu}\bar{l}$, where $\bar{\nu}$ and $\bar{l}$ denote the mean velocity and diffusion length of the reactant, parameters related to temperature, molecular mass and reactant concentration. Diffusion layer thickness δ was determined from the substrate length L and Reynolds value Re by using the equation $\delta = \frac{2L}{3\sqrt{Re}}$.[19] A detailed description and consideration of n^c, D and δ are provided in ESI.†
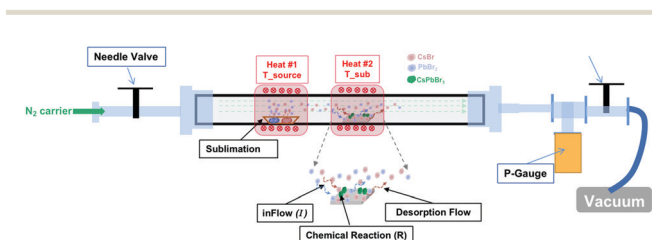

Fig. 1 Schematic diagram of CsPbBr$_3$ perovskite CVD growth.
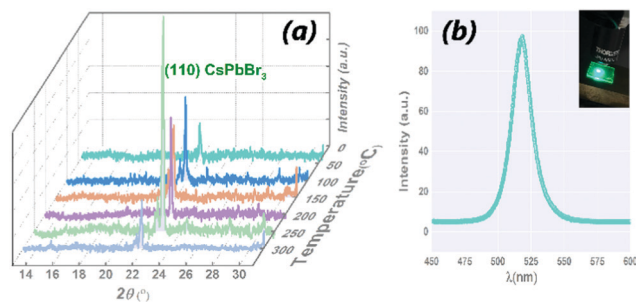

Fig. 2 (a) XRD $2\theta \sim \omega$ scanning of CsPbBr$_3$ films. (b) PL spectrum of CsPbBr$_3$ grown at 250 °C.
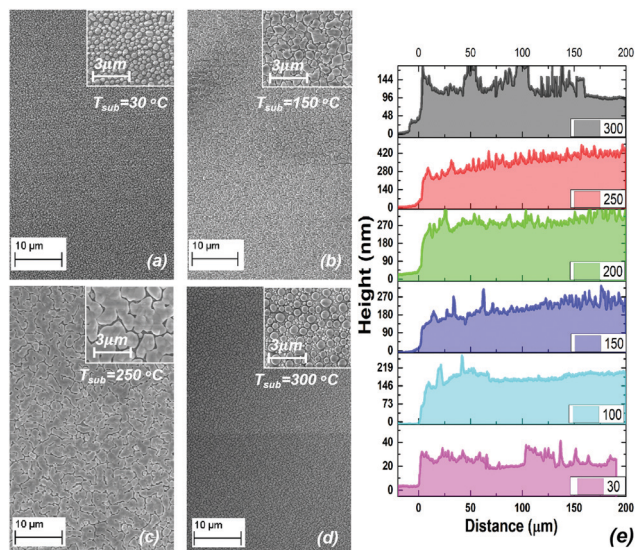
Fig. 3 (a–d) SEM images showing surface morphologies of CsPbBr$_3$ thin films grown at different substrate temperatures, and (e) step scanning profiles of CsPbBr$_3$.

The coefficient of desorption (α) of reactant from substrate was ascribed to the thermal vibration of molecules. Based on the Lindemann criterion,[20] molecules (CsBr and PbBr$_2$) were considered to have desorbed from the substrate when their displacements exceeded 1/10 of the lattice distance. In this work, we estimated the desorption coefficient[21] by using the equation

$$\alpha = f(T,m)\exp\left(-\frac{l_{sf}}{KT}\right), \tag{3}$$

where $f(T,m)$ and l_{sf} denote the vibration frequency and sublimation enthalpy, respectively. The expression for $f(T,m)$ is provided in ESI.†

The chemical reaction CsBr + PbBr$_2$ = CsPbBr$_3$ occurred on the substrate. In eqn (1), the deposition rate (R) was derived from the experimentally measured thickness. Meanwhile, R was determined theoretically from reaction constant A, the activation energy of the chemical reaction E_a, and the concentration of the reactants residing on the substrate[22] by using the equation

$$R = A \cdot \exp\left(-\frac{E_a}{KT}\right) \cdot n_{CsBr}^{sub} \cdot n_{PbBr_2}^{sub}. \tag{4}$$

In this work, we first used the experimental SEM and step profiler data to calculate the deposition rate $R = d \cdot \frac{\mu}{t}$, where d denotes the deposition thickness measured using the stepper, t denotes the deposition time (20 minutes), and μ denotes the

coverage ratio of perovskite determined using SEM. The concentrations of reactants on the substrate (n_{CsBr}^{sub} and $n_{PbBr_2}^{sub}$), desorption coefficients and inflow rates were then calculated by using eqn (1). By obtaining n_{CsBr}^{sub} and $n_{PbBr_2}^{sub}$ at different substrate temperatures, the chemical activation energy was also deduced using eqn (4). Some key parameters used in the calculation are listed in Table 1.

Fig. 4 shows the variation of deposition rates, concentrations of reactants on substrate, and inflow and desorption coefficients for substrate temperatures ranging from 30 °C to 300 °C. The reaction rate peaked at 250 °C, as shown in Fig. 4d. That is, either increasing or decreasing the temperature from this value reduced the deposition rate. This observation could be ascribed to two factors: (1) at low temperature, although n_{CsBr}^{sub} and $n_{PbBr_2}^{sub}$ were high (as shown in Fig. 4a), the chemical reaction rate was limited by temperature with $R \propto \exp\left(-\frac{E_a}{KT}\right)$; (2) at high temperature, $n_{PbBr_2}^{sub}$ was significantly attenuated, which reduced the reaction rate by $R \propto n_{CsBr}^{sub} \cdot n_{PbBr_2}^{sub}$.

As shown in Fig. 4a, n_{CsBr}^{sub} remained nearly constant with increasing substrate temperature, while $n_{PbBr_2}^{sub}$ gradually decreased to a trace amount. n_{CsBr}^{sub} and $n_{PbBr_2}^{sub}$ were related to inflow and desorption. As shown in Fig. 4b, the inflow of PbBr$_2$ (I_{PbBr_2}) was much greater than that of CsBr (I_{CsBr}) when the temperature exceeded 150 °C. This result may have been due to a couple of factors: (1) the lower vaporization temperature and sublimation enthalpy of PbBr$_2$ (917 °C@1atom and 20.75 kJ mol^{-1}) than of CsBr (1300 °C@1atom and 23.64 kJ mol^{-1}), with this factor having made $n_{PbBr_2}^{c}$ nearly double n_{CsBr}^{c} at 300 °C; and (2) a higher diffusion coefficient of PbBr$_2$ (0.4 cm^2 s^{-1}) than of CsBr (0.0395 cm^2 s^{-1}) at 300 °C, with this factor facilitating diffusion of PbBr$_2$ into the substrate.

However, the PbBr$_2$ desorption coefficient (i.e., α_{PbBr_2}) was about 4 to 7 orders of magnitude greater than the CsBr desorption coefficient (α_{CsBr}), which led to low values of $n_{PbBr_2}^{sub}$ at high temperatures. The much greater desorption of PbBr$_2$ than of CsBr resulted from the lower sublimation enthalpy l_{sf} of PbBr$_2$ (136.7 kJ mol^{-1}) than of CsBr (174.3 kJ mol^{-1}). It is worth noting that in our calculation, some parameters (e.g., diffusion velocity and diffusion layer thickness δ of carrier gas) were related to the furnace geometry, while major parameters were not. Therefore, our simulation presented a general in-depth picture of the CVD mechanism.

According to the Arrhenius theory, a chemical reaction needs to overcome an activation energy E_a to achieve the resultant product. Considering the derived n_{CsBr}^{sub}, $n_{PbBr_2}^{sub}$ and deposition rate, E_a of the CVD-grown CsPbBr$_3$ reaction

Table 1 Parameters used in the molecular dynamics equations calculations[23]

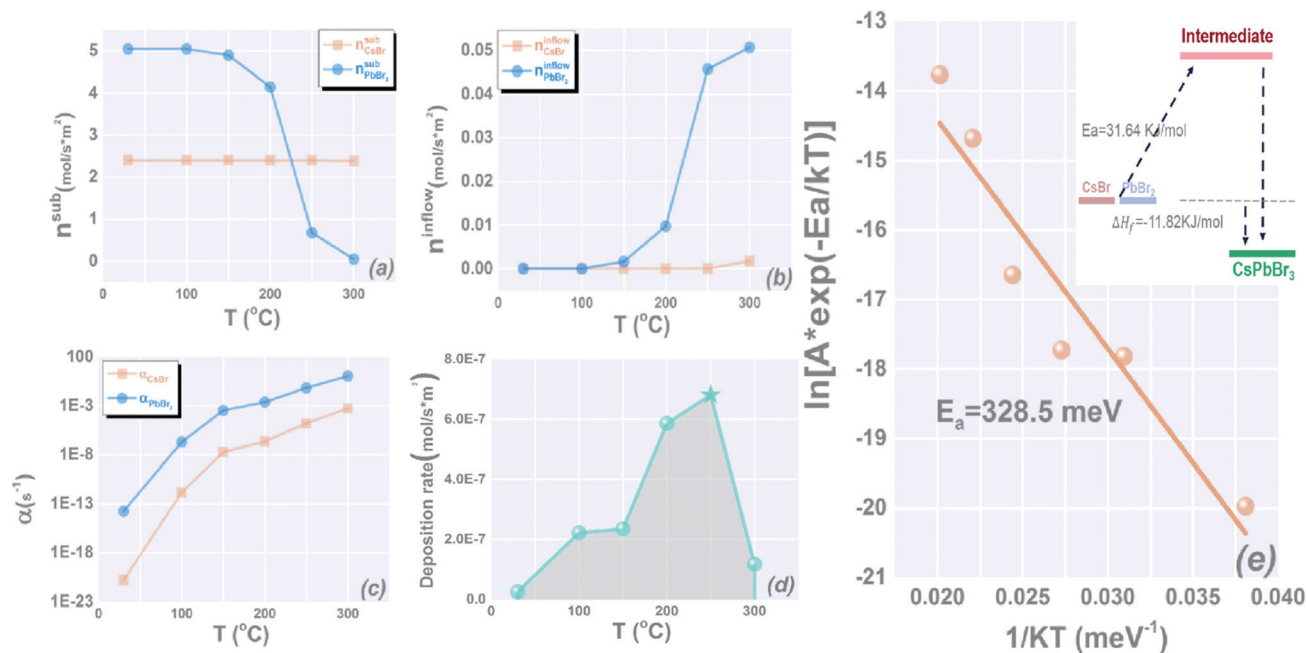| Reactant	Boiling T@1atom (°C)	Molar density (g mol^{-1})	Molecular size (nm)	Sublimation enthalpy (kJ mol^{-1})	Vaporization enthalpy (kJ mol^{-1})
CsBr	1300	212.8	0.382	174.3	23.6
PbBr$_2$	910	367	0.717	136.7	20.8

Fig. 4 (a–c) Simulation results for (a) the concentrations of reactants on the substrate, (b) inflow rates, and (c) desorption coefficients. (d) Experimental deposition rates and (e) fitting curve of the derived activation energy of the chemical reaction.

($CsBr$ + $PbBr_2$ = $CsPbBr_3$) could be deduced using eqn (4), as shown in Fig. 4e. The E_a was determined from fitting to be 328.5 ± 51.5 meV (31.64 ± 15.6 kJ mol^{-1}). The enthalpy of formation of $CsPbBr_3$ from $CsBr$ and $PbBr_2$ was determined to be -11.82 kJ mol^{-1},[24] and this information was used to draw the energy level diagram of the CVD reaction as shown in the inset to Fig. 4e. The reaction apparently first overcame an activation energy of 31.64 kJ mol^{-1}, and then released 43.46 kJ mol^{-1} of energy to form $CsPbBr_3$.

Conclusions

In this work, pure $CsPbBr_3$ perovskite thin films were deposited on quartz substrates at various temperatures using CVD. The highest deposition rate was observed at a 250 °C substrate temperature. Equations of $CsBr$ and $PbBr_2$ on the substrate were derived to investigate the CVD dynamics, and considered the inflow, desorption and chemical reaction processes. At temperatures lower than 250 °C, the deposition rates were limited by the chemical reaction coefficient with an activation energy $E_a = 31.64 \pm 15.6$ kJ mol^{-1}. At temperatures higher than 250 °C, the deposition rate was constrained by high desorption coefficient of $PbBr_2$ due its lower sublimation enthalpy. Our work has provided an in-depth picture for perovskite CVD growth, benefiting further optimization of and research into this technique.

Author contributions

Prof. Hao Long conceived the idea for the work, supervised the work, and acquired funding support for the work. C. Y. Bao performed the sample preparation and measurements and wrote the draft of the manuscript. X. Peng and Y. Mei performed some of the measurements. L. Y. Ying and Prof. B. P. Zhang provided the study materials.

Conflicts of interest

There are no conflicts to declare.

Acknowledgements

References

1 A. Kojima, K. Teshima, Y. Shirai and T. Miyasaka, Organmetal Halide perovskites as visible light sensitizers for photovoltaic cells, *J. Am. Chem. Soc.*, 2009, **131**, 6050.

2 N. J. Jeon, J. H. Noh, W. S. Yang, Y. C. Kim, S. C. Ryu, J. W. Seo and S. I. Seok, Compositional engineering of perovskite materials for high-performance solar cell, *Nature*, 2015, **517**, 476–480.

3 H. P. Zhou, Q. Chen, G. Li, S. Luo, T. B. Song, H. S. Duan, Z. R. Hong, J. B. You, Y. S. Liu and Y. Yang, Interface engineering of high efficient perovskite solar cell, *Science*, 2014, **345**, 542.

4 K. B. Lin, J. Xing, L. N. Quan, F. P. Garcia, X. W. Gong, J. X. Lu, L. Q. Xie, W. J. Zhao, D. Zhang, C. Z. Yan, W. Q. Li, X. Y. Liu, Y. Lu, J. Kirman, E. H. Sargent, Q. H. Xiong and

Z. H. Wei, Perovskite light-emitting didodes with external quantum efficiency exceeding 20 percent, *Nature*, 2018, **562**, 245.

5 Y. Cao, N. Wang, H. Tian, J. S. Guo, Y. Q. Wei, H. Chen, Y. F. Miao, W. Zou, K. Pan, Y. R. He, H. Cao, Y. Ke, M. M. Xu, Y. Wang, M. Yang, K. Du, Z. W. Fu, D. C. Kong, D. X. Dai, Y. Z. Jin, G. Q. Li, H. Li, Q. M. Peng, J. P. Wang and W. Huang, Perovskite light-emitting diodes based on spontaneously formed submicrometre-scale structures, *Nature*, 2018, **562**, 249–253.

6 Y. Wang, W. W. Liu, W. Xin, T. T. Zou, X. Zheng, Y. S. Li, X. H. Xie, X. J. Sun, W. L. Yu, Z. B. Liu, S. Q. Chen, J. J. Yang and C. L. Guo, Back-reflected performance-enhanced flexible perovskite photodetectors through substrate texturing with femtosecond laser, *ACS Appl. Mater. Interfaces*, 2020, **12**, 26614.

7 Q. Zhang, R. Su, X. F. Liu, J. Xing, T. C. Sum and Q. H. Xiong, High-quality whispering gallery mode lasing from cesium lead halide perovskite nanoplatelets, *Adv. Funct. Mater.*, 2016, **26**, 6238.

8 National Renewable Energy Laboratory Best Research-Cell Efficiency Charthttps://www.nrel.gov/pv/assets/pdfs/best-research-cell-efficiencies.20200803.pdf.

9 X. Li, Y. Wu, S. Zhang, B. Cai, J. Gu, J. Song and H. Zeng, $CsPbX_3$ Quantum Dots for Lighting and Displays: Room-Temperature Synthesis, Photoluminescence Superiorities, Underlying Origins and White Light-Emitting Diodes, *Adv. Funct. Mater.*, 2016, **26**, 2435–2445.

10 Q. Pan, H. Hu, Y. Zou, M. Chen, L. Wu, D. Yang, X. Yuan, J. Fan, B. Sun and Q. Zhang, Microwave-Assisted Synthesis of High Quality "All-Inorganic" $CsPbX_3$ (X = Cl, Br, I) Perovskite Nanocrystals and their Application in Light Emitting Diodes, *J. Mater. Chem. C*, 2017, **5**, 10947–10954.

11 Y. Tong, E. Bladt, M. F. Ayguler, A. Manzi, K. Z. Milowska, V. A. Hintermayr, P. Docampo, S. Bals, A. S. Urban, L. Polavarapu and J. Feldmann, Highly Luminescent Cesium Lead Halide Perovskite Nanocrystals with Tunable Composition and Thickness by Ultra sonication, *Angew. Chem., Int. Ed.*, 2016, **55**, 13887–13892.

12 M. B. Faheem, B. W. Khan, C. Feng, M. U. Farooq, F. Raziq, Y. Q. Xiao and Y. B. Li, All-inorganic perovskite solar cell: energetics, key challenges, and strategies toward commercialization, *ACS Energy Lett.*, 2020, **5**, 290–320.

13 Y. Wang, F. Yang, X. Li, F. Ru, P. Liu, L. Wang, W. Ji, J. Xia and X. Meng, Epitaxial Growth of Large-Scale Orthorhombic $CsPbBr_3$ Perovskite Thin Films with Anisotropic Photoresponse Property, *Adv. Funct. Mater.*, 2019, **29**, 1904913.

14 J. A. Raiford, S. T. Oyakhire and S. Bent, Applications of Atomic Layer Deposition and Chemical Vapor Deposition for Perovskite Solar Cells, *Energy Environ. Sci.*, 2020, **13**, 1997–2023.

15 C. Mortan, T. Hellmann, M. Buchhorn, M. d'Eril Melzi, O. Clemens, T. Mayer and W. Jaegermann, Preparation of Methylammonium Lead Iodide ($CH_3NH_3PbI_3$) Thin Film Perovskite Solar Cells by Chemical Vapor Deposition Using Methylamine Gas (CH_3NH_2) and Hydrogen Iodide Gas, *Energy Sci. Eng.*, 2020, 1–9.

16 A. Goktas, A. Tumbul, Z. Aba, A. Kilic and F. Aslan, Enhancing crystalline/optical quality, and photoluminescence properties of the Na and Sn substituted ZnS thin films for optoelectronic and solar cell applications; a comparative study, *Opt. Mater.*, 2020, **107**, 110073.

17 A. Tumbul, F. Aslan, A. Goktas, M. Z. Zarbali and A. Kilic, Highly stable ethanol-based Cu_2ZnSnS_4 (CZTS) low-cost thin film absorber: Effect of solution aging, *Mater. Chem. Phys.*, 2021, **258**, 123997.

18 F. Aslan, G. Adam, P. Stadler, A. Goktas, I. H. Mutlu and N. S. Sariciftci, Sol–gel derived In_2S_3 buffer layers for inverted organic photovoltaic cells, *Sol. Energy*, 2014, **108**, 230–237.

19 F. White, *Fluid Mechanics, Viscous flow in ducts*, McGraw-Hill, New York, 4th edn, 2002, ch. 6, pp. 325–423.

20 S. Rabinovich, A. Voronel and L. Peretzman, Generalization of the lindemann criterion for disordered mixed crystals, *J. Phys. C: Solid State Phys.*, 1988, **21**(35), 5943–5952.

21 N. B. Min, *Physical fundamental of crystal growth*, Shanghai Science & Technology Press, 1982, ch. 9, pp. 375–441.

22 Department of Inorganic Chemistry, Dalian University of Technology, in *Inorganic Chemistry*, Advanced Education Press, 5th edn, 2006, ch. 3, pp. 43–68.

23 J. A. Dean, J. F. Shang, S. J. Chao and W. M. Xin, *et al.*, *Langes Chemistry Handbook*, Science Press, 13th edn, 1991.

24 B. Wang and A. Navrotsky, Thermodynamic studies of Bromide incorporation into cesium lead iodide, *J. Phys. Chem. C*, 2020, **124**, 8639–8642.